Instabilities of the flow around a cylinder and emission of vortex dipoles

Ziv Kizner[1],†, Viacheslav Makarov[2], Leon Kamp[3] and GertJan van Heijst[3]

[1]Departments of Mathematics and Physics, Bar-Ilan University, Ramat-Gan, 5290002, Israel

[2]Centro Interdisciplinario de Ciencias Marinas, Instituto Politécnico Nacional, La Paz, Baja California Sur 23096, México

[3]Turbulence and Vortex Dynamics Group, Eindhoven University of Technology, PO Box 513, 5600 MB Eindhoven, The Netherlands

Instabilities and long-term evolution of two-dimensional circular flows around a rigid circular cylinder (island) are studied analytically and numerically. For that we consider a base flow consisting of two concentric neighbouring rings of uniform but different vorticity, with the inner ring touching the cylinder. We first study the inviscid linear stability of such flows to perturbations of the free edges of the rings. For a given ratio of the vorticity in the rings, the governing parameters of the problem are the radii of the inner and outer rings scaled on the cylinder radius. In this two-dimensional parameter space, we determine analytically the regions of linear stability/instability of each azimuthal mode $m = 1, 2, \ldots$. In the physically most meaningful case of zero net circulation, for each mode $m > 1$, two regions are identified: a regular instability region where mode m is unstable along with some other modes, and a unique instability region where only mode m is unstable. After the conditions of linear instability are established, inviscid contour-dynamics and high-Reynolds-number finite-element simulations are conducted. In the regular instability regions, simulations of both kinds typically result in the formation of vortical dipoles or multipoles. In the unique instability regions, where the inner vorticity ring is much thinner than the outer ring, the inviscid contour-dynamics simulations do not reveal dipole emission. In the viscous simulation, because viscosity has time to widen the inner ring, the instability develops in the same manner as in the regular instability regions.

Key words: instability, vortex breakdown, vortex flows

1. Introduction

A circular flow with alternating vorticity around a cylinder can be experimentally obtained in a rotating fluid by spinning a vertical cylinder for a reasonably long time and then stopping it abruptly. After stopping the cylinder rotation, the fluid velocity drops sharply to zero at the rigid wall; far enough from the cylinder, the fluid is virtually at rest. Thus, inside the viscous boundary layer (which widens slowly), the vorticity is positive, and outside, next to the boundary layer, negative, and the net circulation of the flow is zero. Such a flow can be stable or not. The instability

† Email address for correspondence: Ziv.Kizner@biu.ac.il

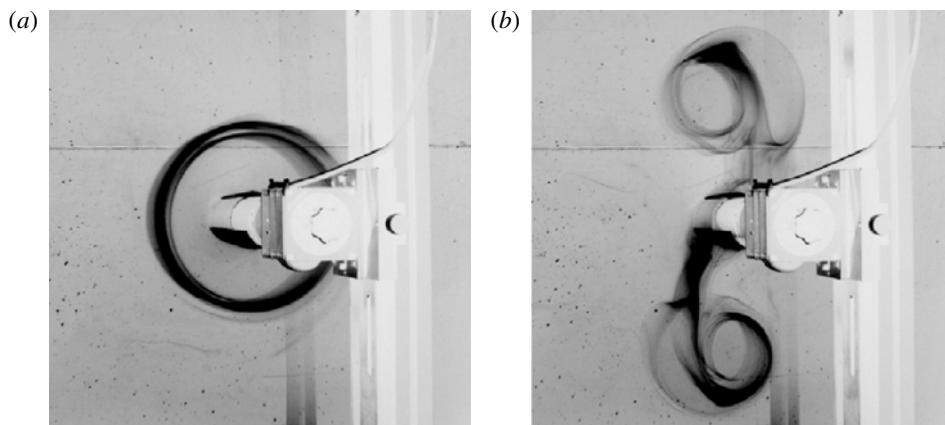(*a*)   (*b*)

FIGURE 1. Unstable evolution of a vortical flow with zero net circulation around a cylinder as observed in an experiment. The flow is induced in a rotating fluid by prolonged spinning and abrupt stopping of the cylinder; the photographs of dye dispersal are taken from above at a small angle relative to the cylinder axis. (*a*) The flow just before the appearance of the instability; the dark circular strip marks the periphery of the flow. (*b*) Emergence of two vortical dipoles.

manifests itself in that, after some time, the flow begins to lose its circular symmetry, and the vortical structure takes the shape of a rotating ellipse or a curvilinear triangle (azimuthal mode-2 or -3 instability). This process normally culminates in the shedding of two or three vortex dipoles (figure 1).

These observations lead us to the following questions: What are the conditions for a flow around a cylinder to be stable? If the flow is unstable, how long can it survive, i.e. what are the growth rates of its unstable modes, and what vortical patterns can emerge due to the instability? This topic is of oceanographic significance. When an island possesses a topographic 'skirt' (a sufficiently steep bottom slope), potential vorticity contours can be closed thus causing the existence of a closed flow around the island (Pedlosky, Iacono & Napolitano 2009). Also, island-trapped inertial or subinertial waves induced by tidal or planetary waves (Longuet-Higgins 1969, 1970; Brink 1999; Dyke 2005) and tidal rectification (Loder & Wright 1985; Wright & Loder 1985; Chen & Beardsley 1995) may cause the formation of mass-transporting currents around islands. One may expect that, in case of instability, such a current will emit vortex dipoles. Coastal waters near islands are usually rich in chemical and biological material, while the vortex dipoles are normally quite robust and, therefore, can serve as carriers of the trapped material.

The aim of our present study is to establish the conditions for linear instability of a two-dimensional azimuthally symmetric shear flow around a rigid circular boundary and to study the long-term, nonlinear evolution of unstable flows, including the formation of new vortical patterns. We assume that, in terms of vorticity, the unperturbed flow is composed of two concentric neighbouring rings of uniform but different vorticity; this assumption makes feasible the investigation of linear stability analytically in the contour-dynamics framework. In this respect, our formulation has some features in common with the model considered by Flierl (1988) who studied the stability of a 'shielded' circular barotropic vortex with a stepwise vorticity distribution, also referred to as a two-contour Rankine vortex. This and the three-contour Rankine
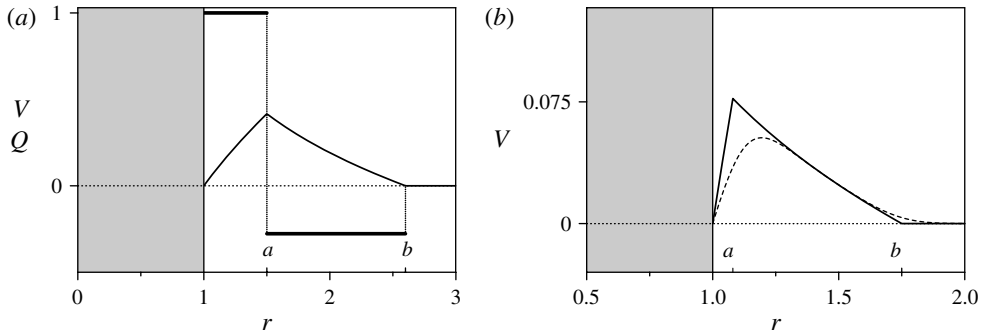
FIGURE 2. Circular flows with zero net circulation ($\Gamma = 0$). (*a*) Theoretical profiles of vorticity Q (bold stepwise line) and velocity V (solid continuous line) determined by (2.1) at $a = 1.5$ and $b = 2.6$. (*b*) The azimuthal velocity profile determined by (2.1) at $a = 1.08$ and $b = 1.75$ (solid continuous line) and that obtained in a simulation with small viscosity ($Re = 3 \times 10^4$) just before the instability (circular asymmetry) becomes visible (smooth dashed line).

vortex were also considered by Kozlov & Makarov (1985*a*,*b*), Carton (1992), Morel & Carton (1994) and Makarov (1996). We first perform the linear stability analysis and subsequently, based on the analytical results, carry out some numerical simulations.

At the stability analysis stage, we regard the fluid to be inviscid and consider the perturbations that affect the free edges of the two rings only. We apply the azimuthal normal-mode approach and determine the regions of stability/instability on the parameter plane spanned by the outer radii of the two rings scaled on the radius of the rigid boundary. The condition of zero net circulation, though relevant to the above-described experiment, does not ease the analysis. The analytical results, therefore, are valid for a flow with an arbitrary stepwise two-ring vorticity profile and zero velocity at the rigid circular boundary. Next, two kinds of numerical simulations are performed, namely, the inviscid contour-dynamics and high-Reynolds-number finite-element simulations, with most attention being given to the zero net circulation case.

2. Linear stability analysis

Consider a two-dimensional circularly symmetric flow around a rigid inner boundary (a circular cylinder). Let the velocity profile of the flow be associated with two rings of uniform vorticity, of which the inner ring touches the cylinder. We shall use the polar coordinates r and θ and regard all the variables and constants to be dimensionless, taking the radius of the cylinder as the length scale and the vorticity and inverse vorticity in the inner ring as the vorticity and time scales, respectively (an alternative time scale is used in § 3.2, where the numerical simulations are discussed). So, the cylinder radius and the vorticity in the inner ring will be taken equal to unity; the vorticity in the outer ring will be denoted as $-\gamma = \text{const}$ (figure 2). Relevant to the experiment mentioned in § 1 is $\gamma > 0$; however, the subsequent analysis does not require specification of the sign of γ. Assuming the two rings to share a common interface contour, we get a stepwise radial vorticity distribution with three contours bounding the rings; in the unperturbed state, these contours are $r = 1$, $r = a$ and $r = b$ (where $1 < a < b$), with the velocity at $r = 1$ being zero (this models the viscous boundary condition at the cylinder, § 1).

Thus, the unperturbed vorticity and azimuthal velocity profiles $Q(r)$ and $V(r)$ are

$$Q(r) = \begin{cases} 1, & 1 \leqslant r < a, \\ -\gamma, & a \leqslant r < b, \\ 0, & b \leqslant r, \end{cases}$$

$$V(r) = \frac{1}{2} \begin{cases} r - 1/r, & 1 \leqslant r < a, \\ -\gamma r + [(1+\gamma)a^2 - 1]/r, & a \leqslant r < b, \\ [-\gamma(b^2 - a^2) + a^2 - 1]/r, & b \leqslant r. \end{cases} \tag{2.1}$$

The subsequent analysis is facilitated by writing Q in terms of the Heaviside step function $H()$,

$$Q(r) = 1 - (1 + \gamma)H(r - a) + \gamma H(r - b). \tag{2.2}$$

The net circulation of the flow is

$$\Gamma = \pi[-\gamma(b^2 - a^2) + a^2 - 1], \tag{2.3}$$

and $\Gamma = 0$ when

$$\gamma = \frac{a^2 - 1}{b^2 - a^2}. \tag{2.4}$$

As seen from (2.1) and (2.4), if $\Gamma = 0$, the velocity outside the contour $r = b$ is identically zero (figure 2), otherwise it drops at infinity as $1/r$. The case of zero net circulation (2.4), therefore, is of special interest as the only case where the net energy of the flow is finite.

In the contour-dynamics framework, perturbations will not affect the values of vorticity within the rings, and only the free interface and the outermost contour are subject to perturbations (the rigid boundary $r = 1$ remains immovable). Thus, we assume that the perturbed vorticity field $\tilde{q}$ is obtained from the base field (2.2) by adding small perturbations $f_a(\theta, t)$ and $f_b(\theta, t)$ to a and b:

$$\tilde{q} = 1 - (1 + \gamma)H[r - (a + f_a(\theta, t)] + \gamma H[r - (b + f_b(\theta, t)]. \tag{2.5}$$

Now decomposing $\tilde{q}$ into a sum $\tilde{q} = Q + q$, where q is a small perturbation, linearizing (2.5) in the neighbourhood of base state Q, and taking into account that

$$\frac{dQ}{dr} = -(1 + \gamma)\delta(r - a) + \gamma\delta(r - b), \tag{2.6}$$

we obtain the expression for the vorticity perturbation in the linear approximation:

$$q = (1 + \gamma)\delta(r - a)f_a(\theta, t) - \gamma\delta(r - b)f_b(\theta, t), \tag{2.7}$$

where $\delta()$ is the Dirac δ-function. Since f_a and f_b are small, q is small in the integral sense.

Any perturbation of the vorticity field is associated with perturbations in the velocity and stream function fields. Let $u = u(r, \theta, t)$ and $v = v(r, \theta, t)$ be the radial and azimuthal components of the velocity perturbation, respectively. In the linear approximation, u (as a function of r) is supposed to be continuous; in contrast, as will be shown below, v will necessarily have jumps at $r = a$ and $r = b$.

The equation of vorticity conservation linearized about the base state is

$$\frac{\partial q}{\partial t} + \frac{1}{r}V(r)\frac{\partial q}{\partial \theta} + u\frac{dQ}{dr} = 0. \tag{2.8}$$

Because $r = a + f_a(\theta, t)$ and $r = b + f_b(\theta, t)$ are material contours, (2.2), (2.7) and (2.8) imply the following two equations in f_a and f_b:

$$\frac{\partial f_a(\theta, t)}{\partial t} + \frac{1}{a} V(a) \frac{\partial f_a(\theta, t)}{\partial \theta} - u(a, \theta, t) = 0, \tag{2.9}$$

$$\frac{\partial f_b(\theta, t)}{\partial t} + \frac{1}{b} V(b) \frac{\partial f_b(\theta, t)}{\partial \theta} - u(b, \theta, t) = 0. \tag{2.10}$$

A formal way to get (2.9) and (2.10) is to substitute into (2.8) the expressions

$$\frac{\partial q}{\partial t} = (1 + \gamma)\delta(r - a) \frac{\partial f_a(\theta, t)}{\partial t} - \gamma\delta(r - b) \frac{\partial f_b(\theta, t)}{\partial t}, \tag{2.11}$$

$$\frac{\partial q}{\partial \theta} = (1 + \gamma)\delta(r - a) \frac{\partial f_a(\theta, t)}{\partial \theta} - \gamma\delta(r - b) \frac{\partial f_b(\theta, t)}{\partial \theta} \tag{2.12}$$

obtained by differentiation of (2.7). This substitution yields the equation

$$(1 + \gamma)\delta(r - a) \left[\frac{\partial f_a(\theta, t)}{\partial t} + \frac{1}{r} V(r) \frac{\partial f_a(\theta, t)}{\partial \theta} - u \right]$$

$$- \gamma\delta(r - b) \left[\frac{\partial f_b(\theta, t)}{\partial t} + \frac{1}{r} V(r) \frac{\partial f_b(\theta, t)}{\partial \theta} - u \right] = 0. \tag{2.13}$$

Integration of the left- and right-hand sides of (2.13) over two non-overlapping segments, one of which includes the point $r = a$ and the other includes the point $r = b$, results in (2.9) and (2.10).

The perturbation flow is conveniently represented in terms of the perturbation stream function ψ which is defined as

$$\frac{1}{r} \frac{\partial \psi}{\partial \theta} = -u, \quad \frac{\partial \psi}{\partial r} = v, \tag{2.14}$$

and is related to q via the Poisson equation

$$\nabla^2 \psi = q. \tag{2.15}$$

The next step in the normal-mode linear stability analysis is assuming each of the functions f_a, f_b and ψ to be a complex azimuthal mode-m wave with the complex frequency ω and amplitude $\alpha = \text{const}$, $\beta = \text{const}$ and $\phi(r)$, respectively,

$$f_a = \alpha e^{im(\theta - \omega t)}, \quad f_b = \beta e^{im(\theta - \omega t)}, \quad \psi = \phi(r) e^{im(\theta - \omega t)}; \tag{2.16}$$

here m is an integer and the function $\phi(r)$ is to be specified. More precisely, $\sigma = \text{Re}(\omega)$ is the frequency and $g = m|\text{Im}(\omega)|$ is the growth rate of the unstable mode-m perturbation. From (2.9), (2.10), (2.14) and (2.16) we obtain the following equations in α and β:

$$-\omega\alpha + \frac{1}{a} V(a)\alpha + \frac{1}{a}\phi(a) = 0, \tag{2.17}$$

$$-\omega\beta + \frac{1}{b} V(b)\beta + \frac{1}{b}\phi(b) = 0. \tag{2.18}$$

Using (2.7) and (2.16), we reduce (2.15) to an ordinary differential equation in ϕ:

$$\phi'' + \frac{1}{r}\phi' - \frac{m^2}{r^2}\phi = \alpha(1 + \gamma)\delta(r - a) - \beta\gamma\delta(r - b), \tag{2.19}$$

where primes designate differentiation with respect to r. Thus, in the segments $1 \leqslant r < a$, $a \leqslant r < b$ and $b \leqslant r$, the function ϕ is a linear combination of r^m and r^{-m}.

Along with (2.14) and (2.16), the boundary conditions $u = 0$ at $r = 1$ and $u, v \to 0$ at infinity involve:

$$\phi(0) = 0, \quad \phi \to 0 \quad \text{at } r \to 0. \tag{2.20}$$

Since u should be continuous, the matching conditions

$$\phi(a-) = \phi(a+), \quad \phi(b-) = \phi(b+) \tag{2.21}$$

must be obeyed. Two more conditions which a solution to (2.19) necessarily satisfies are obtained by integrating the left- and right-hand sides of (2.19) in the intervals $a - \chi \leqslant r \leqslant a + \chi$ and $b - \chi \leqslant r \leqslant b + \chi$ as $\chi \to 0$ and by using (2.21):

$$\phi'(a+) - \phi'(a-) = \alpha(1 + \gamma), \quad \phi'(b+) - \phi'(b-) = -\beta\gamma. \tag{2.22}$$

Thus, the perturbation of the tangential velocity component has jumps at $r = a$ and $r = b$.

The solution to (2.19) that obeys conditions (2.20)–(2.22) is:

$$\phi(r) = \begin{cases} C(r^m - r^{-m}), & 1 \leqslant r < a, \\ Dr^m + Er^{-m}, & a \leqslant r < b, \\ Fr^{-m}, & b \leqslant r, \end{cases} \tag{2.23}$$

where the coefficients C, D, E and F are functions of the parameters a, b, m, α, β and γ:

$$C = \frac{1}{2m}\left[\frac{1}{b^{m-1}}\beta\gamma - \frac{1}{a^{m-1}}\alpha(1+\gamma)\right], \quad D = \frac{1}{2m}\frac{1}{b^{m-1}}\beta\gamma, \tag{2.24}$$

$$\left.\begin{aligned} E &= -\frac{1}{2m}\left[\frac{1}{b^{m-1}}\beta\gamma + \frac{a^{2m}-1}{a^{m-1}}\alpha(1+\gamma)\right], \\ F &= \frac{1}{2m}\left[\frac{b^{2m}-1}{b^{m-1}}\beta\gamma - \frac{a^{2m}-1}{a^{m-1}}\alpha(1+\gamma)\right]. \end{aligned}\right\} \tag{2.25}$$

Using (2.1), (2.24) and (2.25) we can now write the expressions for $V(a)/a$, $V(b)/b$, $\phi(a)/a$ and $\phi(b)/b$ that appear in (2.17) and (2.18):

$$\frac{1}{a}V(a) = \frac{1}{2}\frac{a^2-1}{a^2}, \quad \frac{1}{b}V(b) = \frac{1}{2}\frac{-\gamma(b^2-a^2)+a^2-1}{b^2}, \tag{2.26}$$

$$\frac{1}{a}\phi(a) = -\frac{1}{2m}\frac{a^{2m}-1}{a^{2m}}(1+\gamma)\alpha + \frac{1}{2m}\frac{a^{2m}-1}{a^{m+1}b^{m-1}}\gamma\beta, \tag{2.27}$$

$$\frac{1}{b}\phi(b) = -\frac{1}{2m}\frac{a^{2m}-1}{a^{m-1}b^{m+1}}(1+\gamma)\alpha + \frac{1}{2m}\frac{b^{2m}-1}{b^{2m}}\gamma\beta. \tag{2.28}$$

Substitution of (2.26)–(2.28) into (2.17) and (2.18) and grouping of the terms with the common factors α and β yields two linear homogeneous equations in α and β,

$$(A_1 - \omega)\alpha + B_1\beta = 0, \tag{2.29}$$

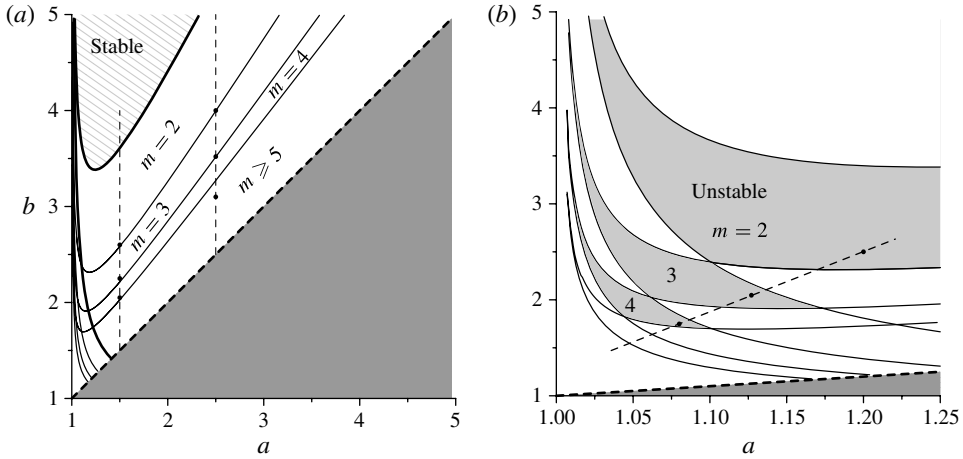$$A_2\alpha + (B_2 - \omega)\beta = 0, \tag{2.30}$$

FIGURE 3. Regions on the (a,b)-plane, in which azimuthal modes $m = 2$, 3, 4 and $m \geqslant 5$ are unstable, $\Gamma = 0$ (zero net circulation). (*a*) General view. (*b*) Magnified regions of unique instability (lighter shaded). Solid circles on dashed straight lines label the states used to initialize the numerical simulations; the darker shaded area beneath the bold dashed line is the area of invalid combinations of a and b.

where the four coefficients A_1, B_1, A_2 and B_2 are given by the following formulae:

$$A_1 = \frac{1}{2} \frac{a^2 - 1}{a^2} - \frac{1}{2m} \frac{a^{2m} - 1}{a^{2m}}(1 + \gamma), \quad A_2 = -\frac{1}{2m} \frac{a^{2m} - 1}{a^{m-1}b^{m+1}}(1 + \gamma), \quad (2.31)$$

$$B_1 = \frac{1}{2m} \frac{a^{2m} - 1}{a^{m+1}b^{m-1}}\gamma, \quad B_2 = \frac{1}{2} \frac{a^2 - 1 - \gamma(b^2 - a^2)}{b^2} + \frac{1}{2m} \frac{b^{2m} - 1}{b^{2m}}\gamma. \quad (2.32)$$

The solvability condition for the linear homogeneous equations (2.29) and (2.30),

$$\omega^2 - (A_1 + B_2)\omega + (A_1 B_2 - A_2 B_1) = 0, \quad (2.33)$$

determines the eigenvalues (complex frequencies ω in (2.16)) as functions of m, a, b and γ:

$$\omega = \tfrac{1}{2}[(A_1 + B_2) \pm \sqrt{\mathscr{D}}], \quad (2.34)$$

where

$$\mathscr{D}(m, a, b, \gamma) = (A_1 + B_2)^2 - 4(A_1 B_2 - A_2 B_1). \quad (2.35)$$

The instability condition is $\mathscr{D} < 0$, whereas the mode-m frequency σ and growth rate g are

$$\sigma(m, a, b, \gamma) = \tfrac{1}{2}(A_1 + B_2), \quad g(m, a, b, \gamma) = \tfrac{1}{2}m\sqrt{|\mathscr{D}(m, a, b, \gamma)|}. \quad (2.36)$$

At $m = 1$ we get $A_1 B_2 - A_2 B_1 = 0$ and $A_1 + B_2 \neq 0$, so $\mathscr{D}(1, a, b, \gamma) > 0$. Thus, mode 1 is linearly stable independently of a, b and γ.

In figures 3 and 4, the regions of instability of modes 2, 3, 4 and $m \geqslant 5$ are shown for three cases, where the net circulation Γ is zero, $-\pi$ and $+\pi$ (see (2.3)). A comparison of the three stability diagrams indicates that the instability regions at $\Gamma = -\pi$ are simply connected and at $\Gamma \geqslant 0$, generally, are not.

One more observation is that the limit of a and b going to infinity is equivalent to the limit wherein the circular cutout in the (x, y)-plane shrinks into a point (in which
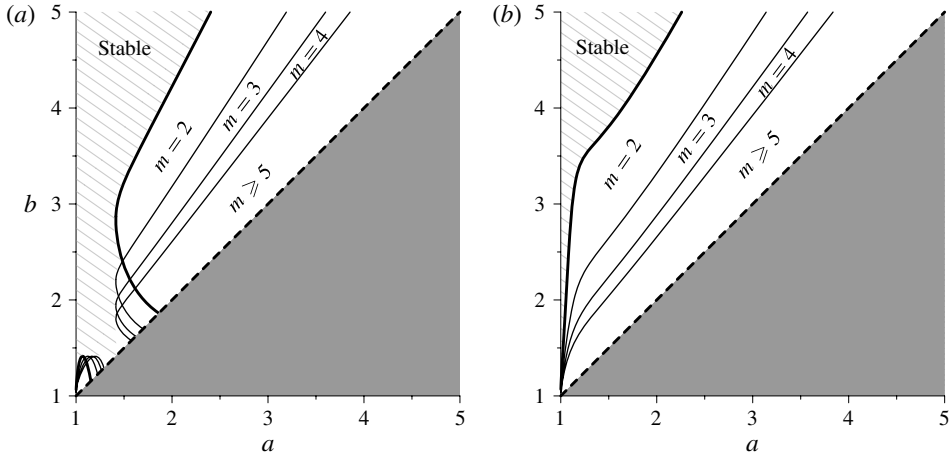
FIGURE 4. Regions on the (a,b)-plane in which azimuthal modes $m = 2$, 3, 4 and $m \geqslant 5$ are unstable. (*a*) $\Gamma = \pi$, (*b*) $\Gamma = -\pi$. Shaded area beneath the bold dashed line, invalid combinations of a and b.

the flow velocity vanishes). In this limit, the pair of concentric vorticity rings becomes a uniform-vorticity shielded monopole, which can be thought of as a superposition of two concentric circular patches of uniform vorticity. Therefore, the boundaries of the stability/instability regions determined by the condition $\mathscr{D} = 0$ (with $\mathscr{D}$ given by (2.35)) should approach asymptotically the rays $b/a = \text{const}$ (different constants for different m) representing the stability bounds for shielded monopoles, which were established by Flierl (1988). A direct analytical calculation based on (2.31), (2.32) and (2.35) confirms that this is indeed the case (figures 3*a* and 4).

From this point on, the physically most meaningful case of finite energy, i.e. of zero net circulation, $\Gamma = 0$, is considered.

For each mode $m \geqslant 2$, we identify two regions of instability in the parameter space, a so-called *regular instability region* where mode m is unstable along with some other modes and a *region of unique instability* where only mode m is unstable (figures 3 and 5). In the case of $m = 2$, both of these regions stretch to infinity, so neither a nor b is limited from above, and only higher unstable modes are found in the regular stability region. At $m > 2$ in the unique instability regions, parameter a is limited ($a < 1.175$), while b is not, and the inner ring is much thinner than the outer one (figure 2*b*). In the latter case, the growth rate of a specific mode is one or two orders of magnitude lower than the typical growth rates in the regular instability region for $a < 1.5$ (figure 5). If a is small enough, then at any $b = \text{const}$ the growth rates decrease with decreasing a. In the next section, contour-dynamics and high-Reynolds-number numerical simulations in the regions of regular and unique instability are discussed.

3. Numerical simulations

3.1. *Methods*

To examine the nonlinear evolution of unstable flows with the profiles given by (2.1), we apply two alternative techniques, contour-dynamics simulations and high-Reynolds-number finite-element simulations, for which identical initial conditions are set based on the analytical results. In both cases, we consider nine examples (see figures 3
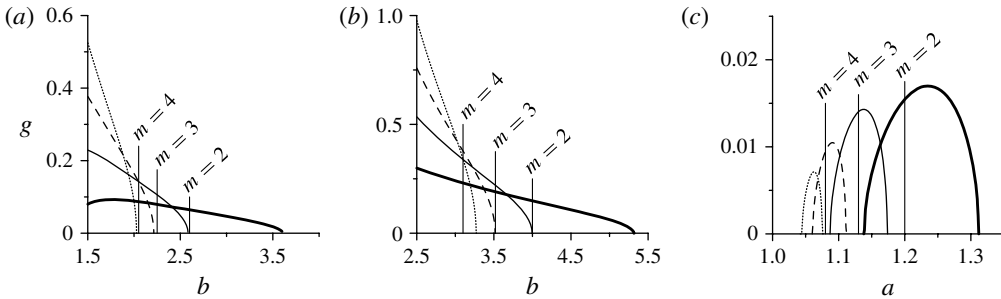
FIGURE 5. Growth rates of unstable modes at the cross-sections shown by dotted straight lines in figure 3 ($\Gamma = 0$) (*a*) at $a = 1.5$, (*b*) at $a = 2.5$, (*c*) through the regions of unique instability. Bold, solid, dashed and dotted lines represent mode 2, 3, 4 and 5, respectively. Vertical straight lines labelled $m = 2$, $m = 3$ and $m = 4$ mark the values of b used to initialize the numerical simulations and indicate the corresponding growth rates.

and 5), in which $\Gamma = 0$. Even though the numerical noise is sufficient to trigger the instability, the growth rates in the regions of unique instability are small (figure 5*c*). Therefore, to accelerate the computations, we slightly perturb the interface and the outermost contours (which originally are $r = a$ and $r = b$) redefining them at $t = 0$ as

$$r = r_a^{(0)} \equiv a \frac{1 + p\sin(m\theta)}{\sqrt{1 + \frac{1}{2}p^2}}, \quad r = r_b^{(0)} \equiv b \frac{1 + p\sin(m\theta)}{\sqrt{1 + \frac{1}{2}p^2}}, \tag{3.1}$$

where m is the number of the azimuthal mode whose instability is to be examined. Although the perturbation factor p in (3.1) is supposed to be small, it is nevertheless finite. The normalization with $\sqrt{1 + p^2/2}$ in (3.1) keeps the areas of the rings (hence, their total circulations) unchanged for any p. In fact, the correction to the $p\sin(m\theta)$ perturbation caused by the normalization is order p^2 and, therefore, is immaterial when p is small enough. The simulations discussed below in § 3.2 were run with $p = 0.005$.

The *contour-dynamics*, or contour-surgery method (Zabusky, Hughes & Roberts 1979; Dritschel 1988; see also Kozlov 1983; Pullin 1992) is widely used for high-resolution simulations of the dynamics of uniform-vorticity patches. Once the shape and location of the contour bounding a uniform-vorticity patch are known, the flow induced by the patch is calculated by inverting the Laplace operator in the Poisson equation that relates the flow stream function and the vorticity field. This calculation implies the use of the Green function $G(x, y; x_0, y_0)$, which can be interpreted as the stream function of a flow induced by a unit point vortex located at a point (x_0, y_0) on the (x, y)-plane, and computation of contour integrals over the patch boundaries. The construction of the Green function in complex domains is often facilitated by the use of image vortices (Coppa, Peano & Peinetti 2002; Johnson & McDonald 2004; Elcrat, Fornberg & Miller 2005; Crowdy & Surana 2007). For a plane with a circular cutout of unit radius centred at the origin of the frame of reference, a Green function can be written as

$$G(x, y; x_0, y_0) = \frac{1}{4\pi}\left[\ln R^2 - \ln\left(\frac{R_0^2 r_0^2}{r^2}\right)\right] \tag{3.2}$$

(e.g. Milne-Thomson 1996; Crowdy 2010), where

$$R^2 = (x - x_0)^2 + (y - y_0)^2, \quad R_0^2 = \left(x - \frac{x_0}{r_0^2}\right)^2 + \left(y - \frac{y_0}{r_0^2}\right)^2, \\ r^2 = x^2 + y^2, \quad r_0^2 = x_0^2 + y_0^2,$$ (3.3)

with $(x_0/r_0^2, y_0/r_0^2)$ being the coordinates of the image vortex inside the circle (recall that all the variables are dimensionless, and the radius of the circle is 1). It is readily verified that this function vanishes at $r = 1$ and goes to a constant limit as $r \to \infty$.

At the initial instant, the two vorticity rings are bounded by the contours $r = 1$, $r = r_a$ and $r = r_b$. With the passage of time the fluid contours may undergo deformations and reconnections due to the surgery (splitting and pooling together of vorticity patches and removal of thin filaments). In our contour-dynamics simulations, to enable the separation of the positive-vorticity area from the cylinder, we consider the innermost contour, just like the interface and outermost contours, as a fluid one. Theoretically, the Green function (3.2) used in our code should keep the normal velocities at the rigid boundary equal to zero, but in practical computations, the accumulation of numerical errors can cause some penetration inside the unit circle of the nodes distributed over the fluid contours. To avoid this unwanted effect (which is in fact very small) we follow the recipe of Macaskill, Padden & Dritschel (2003), i.e. introduce a fictitious border outside the rigid boundary at a short distance ε from it, and bring back to this fictitious border any node that enters the gap between the two borders. Thus, the code is characterized by four parameters, Δt, Δl, ΔS and ε representing, respectively, the time step, the distance between two neighbouring nodes on a contour, the area critical for patch removal, and the distance between the rigid boundary and the fictitious border; $\Delta l/8$ serves as the width of a filament critical for reconnection. By varying the parameters Δt, Δl, ΔS and ε, we found that quite high resolution at reasonable expenditure of time of computations can be achieved with $\Delta t = 0.005$, $\Delta l = 0.03$ (which corresponds to 210 nodes over a circle of a unit radius), $\Delta S = 0.005\pi$, and $\varepsilon = 10^{-6}$. These values are used in the contour-dynamics simulations discussed below.

Aiming to study the effect of weak viscosity on the instability of flows with stepwise vorticity profiles (2.1) we apply the COMSOL CFD facility (Comsol AB 2012). It is a finite-element solver for the time-dependent velocity field. We solve an initial-value problem for the Navier–Stokes equations in two dimensions. The integration in time is performed with an implicit second-order backward-difference scheme whose absolute tolerance is 10^{-5} and employing fourth-order integration for the Lagrangian elements used. The fluid is assumed to be incompressible with unit mass density, and the Reynolds number *Re* (inverse non-dimensional viscosity coefficient) is taken equal to 3×10^4. The computations are run for a 40×40 square with a circular cutout of radius 1. At the inner boundary ($r = 1$) we use the no-slip condition. In order to make the effect of the outer boundary as small as possible, we apply the stress-free condition at $x = \pm20$ and $y = \pm20$; the adequacy of the chosen box size is confirmed by experimenting with larger squares. The computational domain is subdivided into five sub-domains that are defined by the inequalities $r > 14$ (region I), $6 < r < 14$ (region II), $r_b < r < 6$ (region III), $r_a < r < r_b$ (region IV), and $1 < r < r_a$ (region V). All of the five sub-domains are discretized with an unstructured mesh consisting of triangular elements (approximately 4.5×10^6 mesh elements in total). The typical mesh element size in these sub-domains decreases from 0.2 in region I to 0.004 in region IV and then to 0.002 in region V. In order to resolve fine-

scale structures that might emerge close to the no-slip wall ($r = 1$), the mesh-element size close to this boundary is taken as 0.001. The resulting number of degrees of freedom solved for is approximately 15×10^6. The integration in time is initialized with the velocity field that complies with the stepwise vorticity distribution subjected to the perturbation (3.1).

There are different ways to compute the initial velocity field. The method employed in our simulations is appropriate for the case of zero net circulation, $\Gamma = 0$, considered below. We solve the Poisson equation for the stream function Ψ with the source term given by the first of (2.1) with $r_a^{(0)}$ and $r_b^{(0)}$ replacing a and b (see (3.1)), the boundary conditions being $\Psi = 0$ at $r = 1$, $\partial \Psi / \partial x = 0$ at $x = \pm 20$ and $\partial \Psi / \partial y = 0$ at $y = \pm 20$. The velocity field is then obtained by differentiation of Ψ. The choice of the Neumann condition for Ψ at the outer boundary is justified by the fact that, at $\Gamma = 0$, the flow velocity at the outer boundaries is negligibly small. Indeed, in the absence of perturbation, the velocity at $r > b$ is identically zero (see (2.1) and (2.4)). The small perturbation (3.1) imposed on the vorticity distribution causes the presence of a small perturbation in the stream function outside the vorticity rings. According to (2.23), (2.25) and (3.1), with increasing r, this perturbation decreases as $F/r^m \sim p/r^m$, and the velocity as p/r^{m+1} (see (2.16)). Thus, for $p = 0.005$, the velocity at the boundaries $x, y = \pm 20$ is order 10^{-6} or less.

3.2. *Results and discussion*

We present here the results for the case of zero net circulation, $\Gamma = 0$. The parameters of the initial states are labelled in figure 3 by solid circles, and the expected growth rates of linear instability are shown in figure 5. So, for each numerical method, the results of nine simulations are shown, grouped in three series.

In the contour-dynamics simulations (figures 6–8), three main scenarios can be distinguished. In the first series (figure 6), the width of the inner ring is 0.5, while the width of the outer ring, remaining comparable with the width of the inner ring, decreases with increasing m from 1.1 at $m = 2$ to 0.55 at $m = 4$ (figures 3a and 5a). Accordingly, the absolute value of the vorticity in the outer ring, $|\gamma|$, increases approximately from 0.28 to 0.64. In all of the three cases considered, $m = 2$, 3 and 4, the emergence of m dipoles is observed (figure 6).

In the second series (figure 7), the width of the inner ring is 1.5. Here, as m increases from 2 to 4, the width of the outer ring decreases from 1.5 to 0.6, i.e. to approximately one-third of the width of the inner ring (figures 3a and 5b), and $|\gamma|$ increases approximately from 0.54 to 1.56. At $m = 2$, the evolution resembles that in the first series (cf. figures 6a and 7a). In our opinion this is due to the fact that, in both cases, $|\gamma|$ is considerably smaller than 1, the vorticity in the inner ring, while the inner and outer rings are comparably wide. At $m = 4$, where the outer ring is almost three times thinner than the inner one and $|\gamma| \approx 1.56$, the four relatively strong but compact negative-vorticity protuberances tear off only part of the positive-vorticity ring, while the other part remains stuck to the cylinder, thus causing the existence of a counterclockwise flow near the cylinder. The emerged dipoles, being unbalanced, have a clockwise rotation component in their motion, and therefore approach the cylinder (figure 7c). Thus, we observe the formation of a vortex pentapole, an almost four-fold symmetric configuration with a central positive-vorticity ring (whose outer edge tends to take a four-pointed star shape) surrounded with four negative satellite vortices. The whole structure rotates counter-clockwise, with the theoretical frequency σ of the linear wave being a good estimate for the angular velocity. The contour surgery makes the dynamical system non-conservative, thus enabling it to stabilize in a certain state
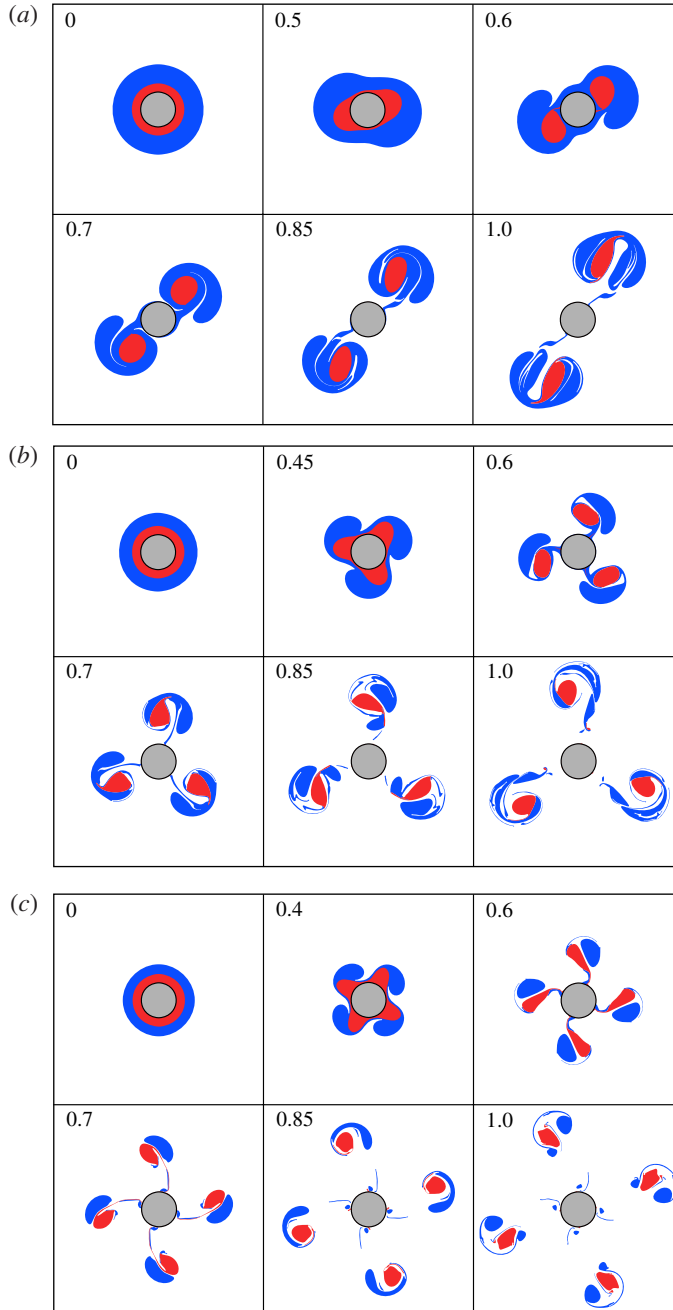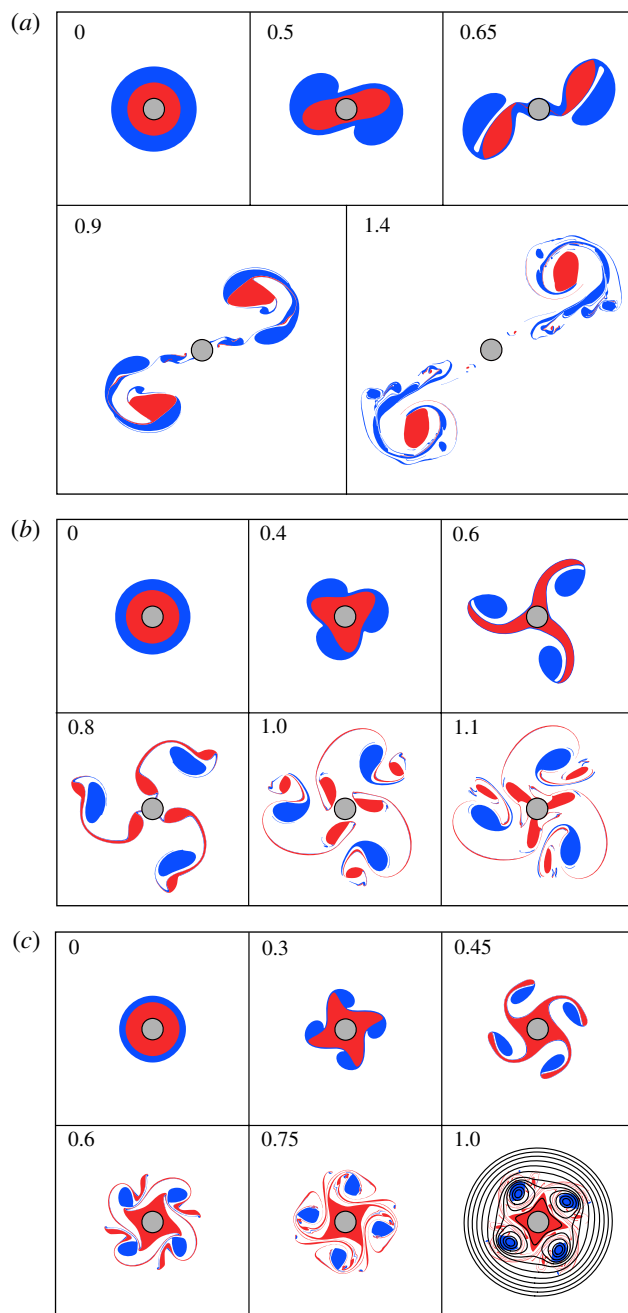
FIGURE 6. (Colour online) Evolution of the vorticity field in the contour-dynamics simulations at $a = 1.5$ and (*a*) $b = 2.6$ ($m = 2$), (*b*) $b = 2.25$ ($m = 3$), (*c*) $b = 2.05$ ($m = 4$). Lighter grey/darker grey patches (red/blue online) mark positive/negative vorticity; light-grey circle in the centre shows the solid cylinder. The parameters (a, b) of the initial states are indicated in figures 3(*a*) and 5(*a*) (regular instability regions). Figures in the corners specify time scaled on $2\pi/\sigma(m, a, b, \gamma)$ (see (2.36) for the definition of σ).

FIGURE 7. (Colour online) Evolution of the vorticity field in the contour-dynamics simulations at $a = 2.5$ and (*a*) $b = 4$ ($m = 2$), (*b*) $b = 3.52$ ($m = 3$), (*c*) $b = 3.1$ ($m = 4$). The parameters (*a*, *b*) are indicated in figures 3(*a*) and 5(*b*) (regular instability regions). Time and grey scale (colour online) as in figure 6; contours in the rightmost lower panel indicate streamlines in the co-rotating frame of reference.
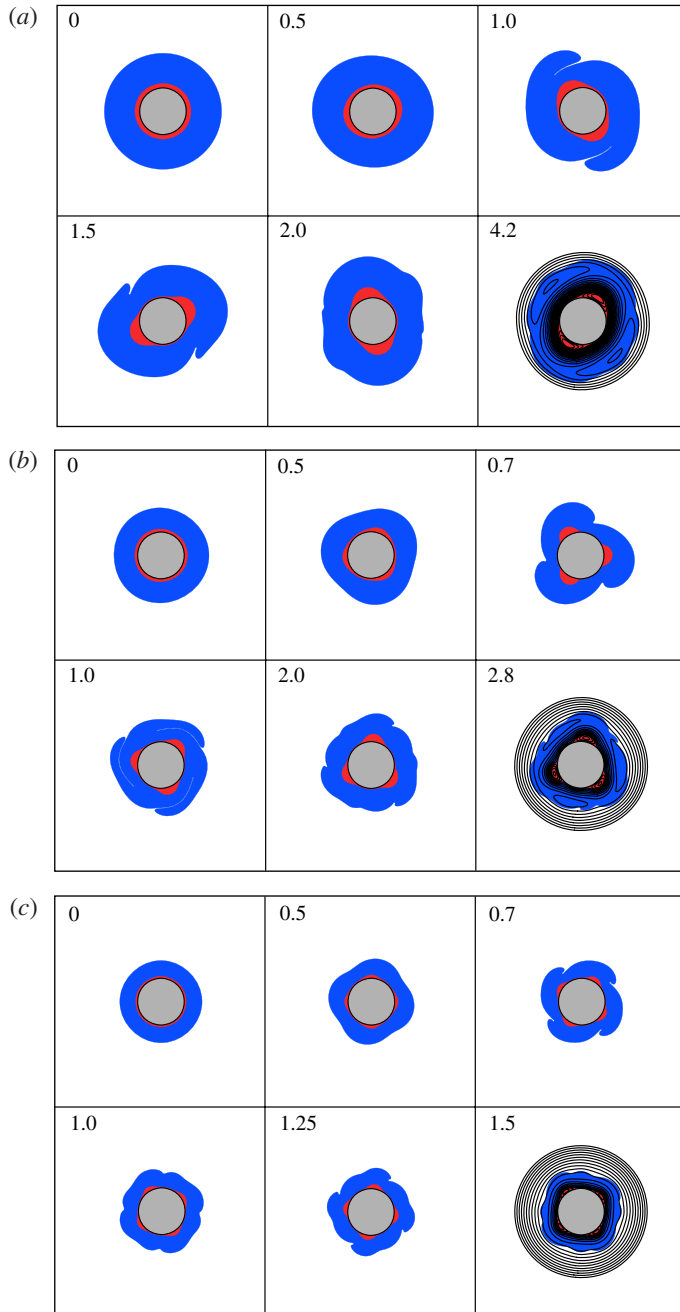
FIGURE 8. (Colour online) Evolution of the vorticity field in the contour-dynamics simulations at (*a*) $a = 1.2$ and $b = 2.5$ ($m = 2$), (*b*) $a = 1.13$ and $b = 2.062$ ($m = 3$), (*c*) $a = 1.08$ and $b = 1.75$ ($m = 4$). The parameters (a, b) of the initial states are indicated in figures 3(*b*) and 5(*c*) (unique instability regions). Time and grey scale (colour online) as in figure 6; contours as in figure 7.
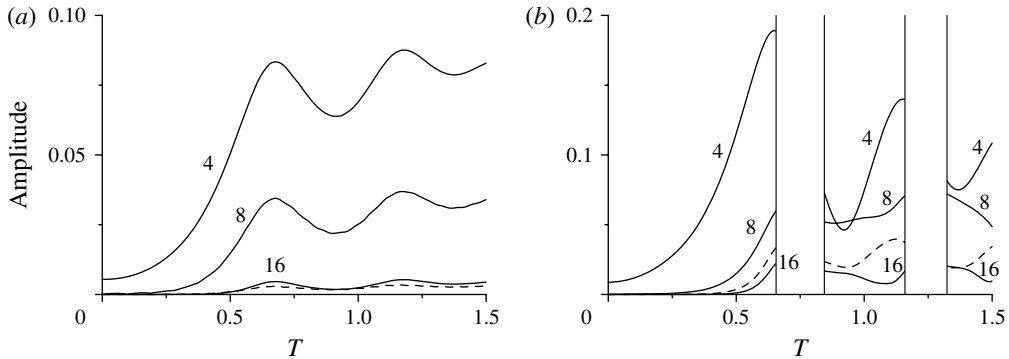
FIGURE 9. Evolution of the amplitudes of the Fourier harmonics comprising the perturbations of the vorticity contours in the simulation at $a = 1.08$ and $b = 1.75$. (*a*) Interface contour; (*b*) outer contour. Solid lines labelled 4, 8 and 16 represent the amplitudes of modes 4, 8 and 16, respectively; dashed line, the mode-12 amplitude. Time (abscissa) is scaled on the theoretical period of the mode-4 wave. The corresponding evolution of the vorticity field is shown in figure 8(*c*).

(compare the shapes of the material contours and the streamlines in figure 7*c*) and not oscillate near to a stable state. The case of $m = 3$ in the second series is intermediate between the two considered above. Here, the dipoles are able to move further away from the cylinder; nevertheless, the tendency to form a quadrupole can be traced here as well (figure 7*b*).

In the third series (unique instability regions), the inner ring is very thin compared to the cylinder and the outer ring. The impact of instability on two such rings is different (figure 8). Whereas the inner ring virtually rearranges into m symmetrically located crescent pieces (connected with thin filaments), the outer ring undergoes moderate deformation, and, depending on m, demonstrates a tendency to take the shape of an ellipse (figure 8*a*), rounded triangle (figure 8*b*) or rounded square (figure 8*c*) with some bulges on the sides. In each of the third-series simulations, no detectable filamentation occurs, and the whole structure tends to oscillate near a steadily rotating state whose angular velocity is close to the initial frequency σ (weak dissipation caused by computational errors may even stimulate convergence to this state). The co-rotating stream function field is more inert than the vorticity distribution; therefore, the streamlines in figure 8 give some idea of these hypothetical steady states.

In the first two series of simulations, where the two vorticity rings are comparably wide, the mode-m waves propagating on both the outer and interface contours can grow until the shape of the two rings is corrupted considerably and m dipoles emerge; subsequently, this may lead to the formation of multipoles (figure 7*c*). The emergence of dipoles and multipoles from two- and three-contour Rankine vortices, respectively, was reported by Kozlov & Makarov (1985*a*), Carton (1992), Morel & Carton (1994) and Makarov (1996).

In the third series (unique instability regions), the instability develops in a fundamentally different way. To better understand this process, as an example, we consider the $m = 4$ case, where $a = 1.08$ and $b = 1.75$, and represent the perturbations $r = r_a(t, \theta) - a$ and $r = r_b(t, \theta) - b$ developing on the interface and the outer contours as series of azimuthal harmonics truncated at harmonic 36 (figure 9). Such a Fourier

expansion can be performed only for the times at which the functions $r_a(t, \theta)$ and $r_b(t, \theta)$ are single-valued; this is why there are voids in the graphs in figure 9(*b*). As we see, at the initial, weakly nonlinear stage the perturbation is bi-modal: it is comprised, in essence, of the leading mode 4 and a resonance mode 8 which grow quasi-exponentially. At a later, significantly nonlinear stage, modes 12 and 16 arise, while the rest of harmonics remain weaker than these.

The inner vorticity ring is very thin at the beginning and touches a fixed inner boundary (at least, at the quasi-exponential stage), while the area occupied by the positive vorticity must be conserved during the evolution. In such circumstances, strong growth of a perturbation on the interface contour would have lead to the formation of high and compact outward crests alternating with long and flattened troughs, i.e. to the growth of both low (4 and 8) and higher modes. A bimodal perturbation, however, cannot take such a shape; accordingly, in our case, the growth of harmonics 4 and 8 is rather limited, and the quasi-exponential phase gives way to the oscillation of the amplitudes near the levels of 0.075 and 0.025, respectively (figure 9*a*).

The perturbations developing on the two contours enter the nonlinear stage simultaneously; in this stage the amplitudes of their harmonics oscillate. As the linear analysis suggests (§ 2), the amplitudes of a specific harmonic wave propagating on the interface and outer contours are comparable. Therefore, at the beginning of the nonlinear stage, the amplitudes of the leading harmonics 4 and 8 in the perturbation developing on the outer contour are approximately 0.2 and 0.05, i.e. are, respectively, 30 % and 8 % of the initial width of the outer ring (figure 9*b*). Close to the moment when the amplitude of harmonic 4 reaches its local maximum, the bulges of the outer ring begin acting as anticyclonic vortices inducing local clockwise motion. This causes the entrainment of the neighbouring zero-vorticity fluid and overturning of the bulges backward relative to the direction of their propagation (figures 9*b* and 8*c*). But due to the relative weakness of the perturbation, i.e. because it does not penetrate deep into the outer ring, this overturning does not lead to the emergence of dipoles, and the outer contour smooths out with time (figures 9*b* and 8*c*). The overturning occurs again close to the moment when the second local maximum is reached (figures 9*b* and 8*c*), and then again the outer contour smooths out. Important in this context is the oscillation of the amplitudes of harmonics 4 and 8 (with signs of slow stabilization at certain levels); note that in a longer simulation, modes 12 and 16 decrease considerably. This fact strengthens our guess regarding the existence of a steady state near which the vortical structure oscillates (and to which it conceivably may converge). To verify this hypothesis we simulated the evolution of a state made up by superimposing upon the unperturbed contours of modes 4 and 8 with the amplitudes estimated based on the Fourier analysis at $T = 2$. The changes in the shape of the vortex structure and in amplitudes of the harmonics in this simulation were relatively small. The existence of a steady state near the developing structure is another, dynamical-systems reading of the early ceasing of the growth of instability.

The development observed in the simulation with $a = 1.08$ and $b = 1.75$ (figure 8*c*) has some resemblance to that in the simulation presented in figure 7(*c*), where the outer ring is noticeably thinner than the inner one, and large part of the positive-vorticity ring remains attached to the rigid cylinder. The fundamental difference, however, is that in the simulation with $a = 1.08$ and $b = 1.75$ the thin ring is sandwiched between the rigid boundary and a massive neighbouring ring, whereas in the simulation with $a = 2.5$ and $b = 3.1$ the thin ring has more freedom since both of its boundaries are fluid.

Three series of simulations with the same parameters as above were run using the finite-element high-Reynolds-number code. In the regular instability regions, i.e. in the first two series where $a = 1.5$ and 2.5 (figures 10 and 11), the same sequence of events as in the contour-dynamics simulations is observed, although one can recognize some time lag (cf. figures 10, 11 and 6, 7). In the unique instability regions (figure 12), however, the evolution differs radically from that observed in the contour-dynamics simulations (cf. figures 12 and 8). Now, one can distinguish two phases in the evolution. In the first phase, the inner vorticity ring slowly increases its width, and in the second phase, the instability appears, culminating in the emission of m dipoles. Note that, in the contour-dynamics simulations, the velocity profile remains practically unchanged as long as the flow remains almost circular.

To discuss the competition between the ring widening and growth of instability in the viscous evolution let us again consider as an example the case of $a = 1.08$ and $b = 1.75$, in which the mode-4 instability results in the emission of four dipoles (figure 12c). Viscosity, both physical and numerical, has a smoothing effect on the velocity profile (figure 2b). This is possibly the cause of the delay in the instability development in the first phase (figures 8c and 12c). The first phase lasts till $T = 0.5$ (figures 2b and 12c), where $T = (\sigma/2\pi)t$ is time normalized by the theoretical period of the mode-4 wave. During this time, which corresponds to 300 units of t, in a purely linear process, the mode-4 perturbation growing with the theoretical growth rate $g \approx 0.01$ (figure 5c) should increase from 0.5% (see (3.2)) to 10% and become pronounced. This is what in essence happens in the contour-dynamics simulation (figures 8c and 9), where harmonic 4 in the perturbation developing on the interface and outer contours reaches, respectively, the levels of 5% and 6.7% (note that some energy goes to the excitation of mode 8 and higher modes, so the process here is weakly nonlinear). In contrast, in the viscous evolution, by $T = 0.5$, the flow is still almost circularly symmetric (figure 12c); Fourier analysis of the vorticity field confirms this observation. The most significant feature, however, is that because the inner front of the velocity profile is initially 8 times (roughly) steeper than the outer one, the viscosity in the inner vorticity ring functions 64 times more efficiently than in the outer ring. Accordingly, by $T = 0.5$, the inner ring widens considerably, while the outer ring does not (some extra widening might occur due to the 'grid viscosity', but this effect is reduced due to the use of an especially fine mesh close to the inner boundary, $r = 1$). The viscous widening proceeds in time according to the square-root law; therefore it can compete with the exponential growth of the linear instability only during a limited time period, namely, within the first phase of evolution. The widening of the inner vorticity ring means that, effectively, parameter a increases from 1.08 to approximately 1.18, while b barely changes (figure 2b). So the point representing the almost circular flow on the (a, b)-plane moves gradually from the region of mode-4 unique instability to the regular instability region of this mode (figure 3b). Therefore the instability develops basically in the same way as in the case $a = 1.5$ and $b = 2.05$, leading to the emission of four dipoles (compare figures 10c and 12c). The same reasoning is applicable to modes 2 and 3 (figure 12a,b).

Close to the inner boundary, $r = 1$, the evolution of the flow field as simulated with the high-Reynolds-number code also differs from that observed in the contour-dynamics simulations. Most remarkable is the occurrence of boundary layer separation, which is visible in some of the snapshots presented in figures 10–12. For example, in figure 10(a) we observe the emergence of two oppositely signed spiky vortical structures at the cylinder. The development of this process is shown in figure 13 at high magnification. Similar behaviour is visible in figure 10(b) at $T = 0.45$
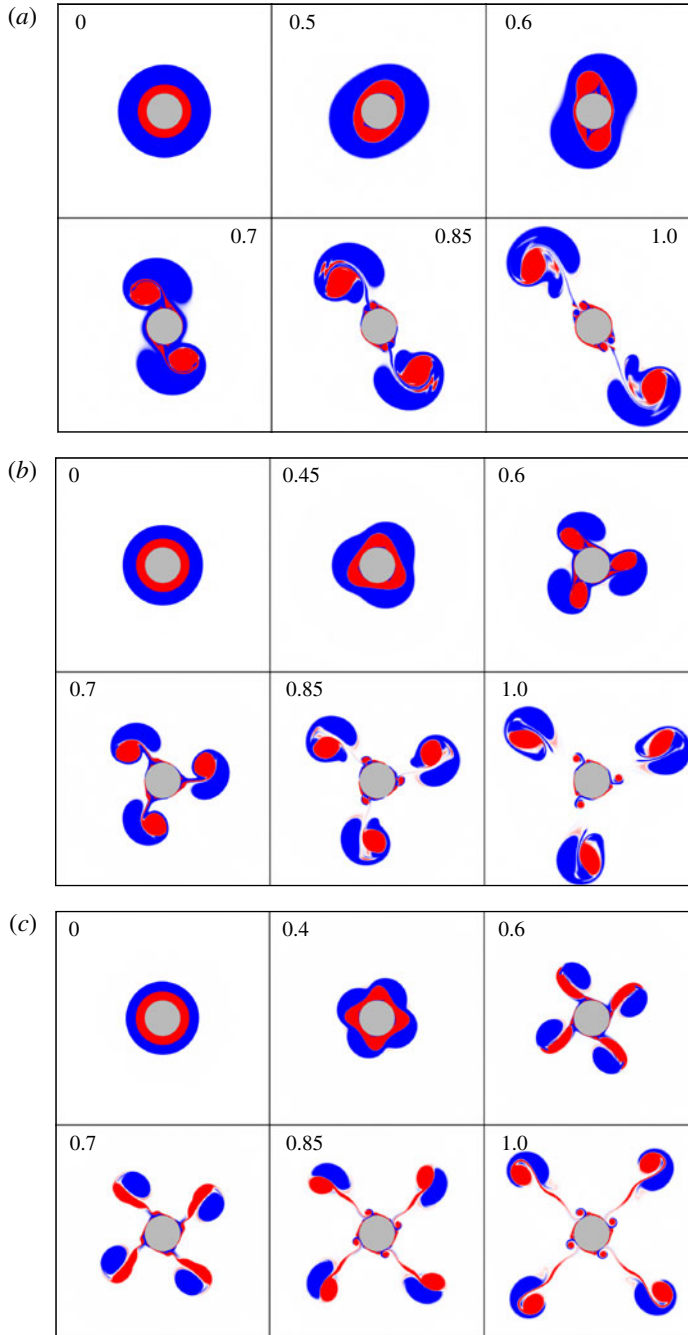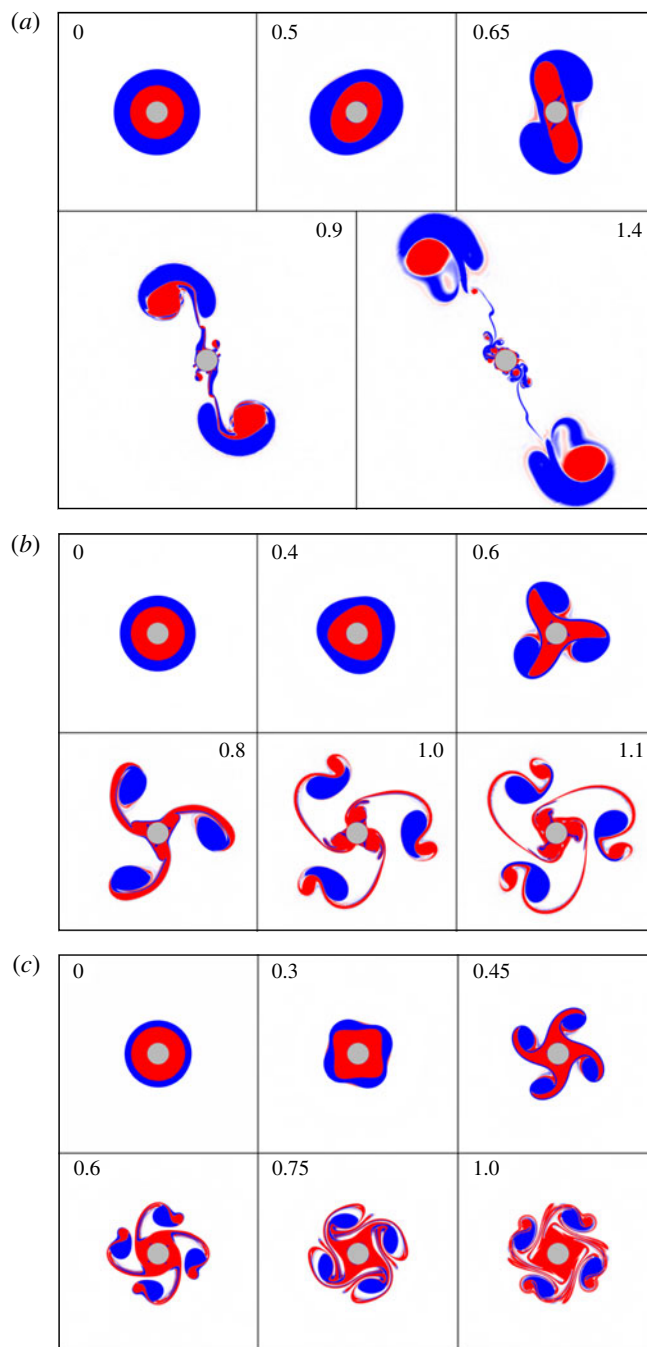
FIGURE 10. (Colour online) Evolution of the vorticity field in the high-Reynolds-number simulations ($Re = 3 \times 10^4$) at $a = 1.5$ and (*a*) $b = 2.6$ ($m = 2$), (*b*) $b = 2.25$ ($m = 3$), (*c*) $b = 2.05$ ($m = 4$). The parameters (a, b) are indicated in figures 3(*a*) and 5(*a*) (regular instability regions). Time and grey scale (colour online) as in figure 6.
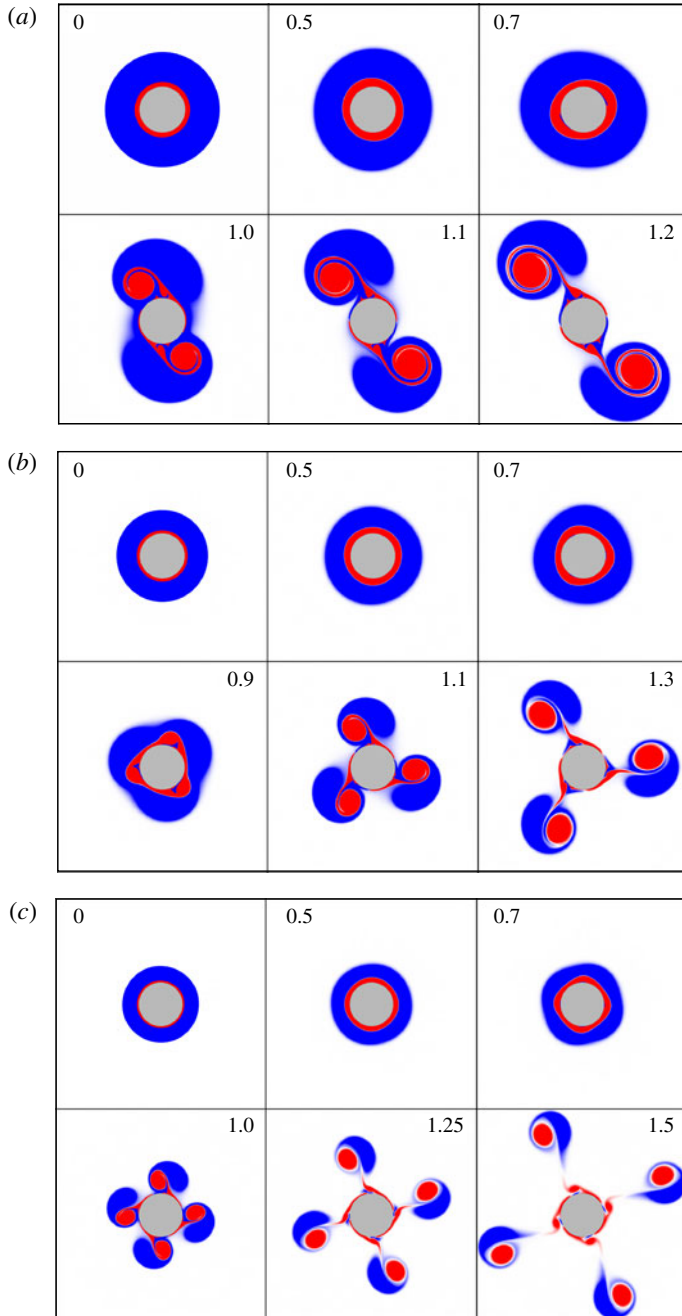
FIGURE 11. (Colour online) Evolution of the vorticity field in the high-Reynolds-number simulations ($Re = 3 \times 10^4$) at $a = 2.5$ and (*a*) $b = 4$ ($m = 2$), (*b*) $b = 3.52$ ($m = 3$), (*c*) $b = 3.1$ ($m = 4$). The parameters (*a*, *b*) are indicated in figures 3(*a*) and 5(*b*) (regular instability regions). Time and grey scale (colour online) as in figure 6.

FIGURE 12. Evolution of the vorticity field in the high-Reynolds-number simulations ($Re = 3 \times 10^4$), at (*a*) $a = 1.2$ and $b = 2.5$ ($m = 2$), (*b*) $a = 1.13$ and $b = 2.062$ ($m = 3$), (*c*) $a = 1.08$ and $b = 1.75$ ($m = 4$). The parameters (a, b) of the initial states are indicated in figures 3(*b*) and 5(*c*) (unique instability regions). Time and grey scale (colour online) as in figure 6.
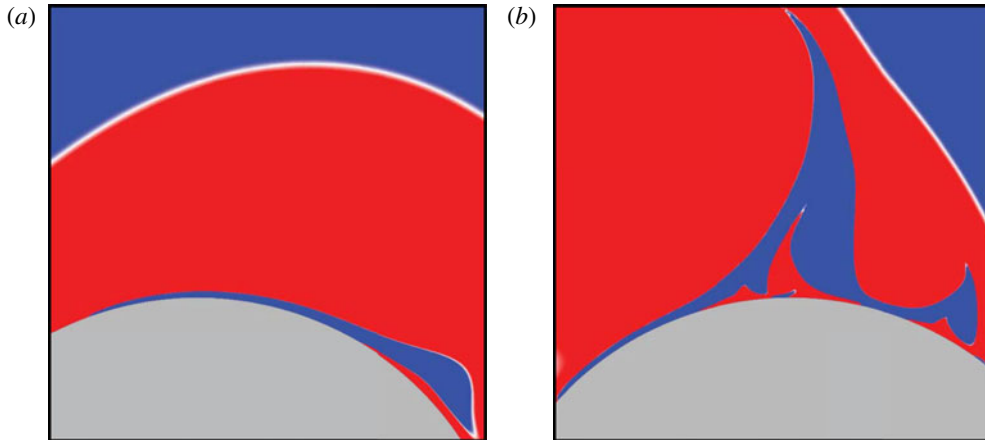
FIGURE 13. (Colour online) Initial and developed stages of the boundary layer separation in the high-Reynolds-number simulation ($Re = 3 \times 10^4$) at $a = 1.5$ and $b = 2.6$. The vorticity field at (*a*) $T = 0.5$ and (*b*) at $T = 0.63$. Grey scale (colour online) as in figure 6.

and $T = 0.6$, in figure 11(*a*) at $T = 0.65$, in figure 11(*b*) at $T = 0.6$, and in figure 12(*b*) at $T = 0.9$. The separation of the boundary layer results from the loss of azimuthal symmetry as the mode-*m* instability develops. This leads to localized flow reversal having *m*-fold symmetry, hence to the boundary-layer separation. Moreover, as the emerged *m* dipoles detach from the cylinder and move away from it, once again oppositely signed vorticity is produced at the no-slip cylinder wall leading to the formation of fine-structure (secondary) dipoles that seem to cling to the cylinder (see e.g. figure 10*a*, $T = 0.86$, $T = 1.0$ and figure 11*a*, $T = 1.4$).

4. Conclusion

By applying the azimuthal normal-mode approach, we determined analytically the regions of flow stability/instability on the (a, b)-plane, where a and b are the outer radii of the two vorticity rings scaled on the radius of the rigid boundary. For the flows with zero net circulation, it is shown that, for any mode $m \geqslant 2$, apart from the region where this mode and some other modes are unstable (we term this region the regular instability region), a region exists in which mode m and only this mode is unstable (the unique instability region). In the unique instability region at $m > 2$, the inner vorticity ring is much thinner than the outer ring.

In order to study the long-term nonlinear evolution of linearly unstable flows, numerical simulations of two kinds were performed: inviscid contour-dynamics simulations and high-Reynolds-number finite-element simulations. The contour-dynamics simulations were made feasible by using the Green function for the Laplace operator on a plane with a circular cutout. To simulate the weakly viscous dynamics, we used the finite-element COMSOL software (Comsol AB 2012).

In the regular instability regions, for two vorticity rings of comparable width, the results obtained with the two techniques are qualitatively the same. Here we observe the emission of dipoles, the number of dipoles being determined by the number of the most unstable mode. When a and b are such that the outer ring is considerably thinner than the inner ring and, therefore, the negative vorticity in it is sufficiently strong, the dipoles are unbalanced thus having a clockwise rotation component in

their motion. Therefore, the dipoles approach the cylinder, tending to form a vortex multipole around it.

In all the simulations carried out for the unique instability regions, the inner ring is considerably thinner than the outer one, and the results depend significantly on which of the two numerical techniques is used. In the contour-dynamics simulations, the vorticity rings undergo considerable deformation, but no dipole emission is observed. The latter is related to the fact that the thin ring is sandwiched between the rigid cylinder and a massive outer ring.

In the finite-element simulations, two phases of evolution can be distinguished. In the first phase, the viscous widening of the inner ring is faster than the growth of instability. This, in effect, moves the point representing the flow in the parameter space (a, b) from the unique instability region into the regular instability region of mode m. As a result, in the second phase, the instability development follows the scenario typical of the regular instability regions. Another, secondary, effect observed in all of the high-Reynolds-number simulations in the vicinity of the rigid cylinder is the separation of the viscous boundary layer at relatively early stages of nonlinear evolution of the flow.

Acknowledgements

REFERENCES

BRINK, K. H. 1999 Island-trapped waves with applications to observations off Bermuda. *Dyn. Atmos. Oceans* **29**, 93–118.

CARTON, X. J. 1992 On the merger of shielded vortices. *Europhys. Lett.* **18**, 697–703.

CHEN, C. & BEARDSLEY, R. C. 1995 A numerical study of stratified tidal rectification over finite-amplitude banks. Part I: symmetric banks. *J. Phys. Oceanogr.* **25**, 2090–2110.

COMSOL AB, 2012 *COMSOL Multiphysics Modelling Guide*. Version 4.3.

COPPA, G. G. M., PEANO, F. & PEINETTI, F. 2002 Image-charge method for contour dynamics in systems with cylindrical boundaries. *J. Comput. Phys.* **182**, 392–417.

CROWDY, D. 2010 A new calculus for two-dimensional vortex dynamics. *Theor. Comput. Fluid Dyn.* **24**, 9–24.

CROWDY, D. & SURANA, A. 2007 Contour dynamics in complex domains. *J. Fluid Mech.* **593**, 235–254.

DRITSCHEL, D. G. 1988 Contour surgery: a topological reconnection scheme for extended contour integrations using contour dynamics. *J. Comput. Phys.* **77**, 240–266.

DYKE, P. 2005 Wave trapping and flow around an irregular near circular island in a stratified sea. *Ocean Dyn.* **55**, 236–247.

ELCRAT, A., FORNBERG, B. & MILLER, K. G. 2005 Stability of vortices in equilibrium with a cylinder. *J. Fluid Mech.* **544**, 53–68.

FLIERL, G. R. 1988 On the stability of geostrophic vortices. *J. Fluid Mech.* **197**, 349–388.

JOHNSON, E. R. & MCDONALD, N. R. 2004 The motion of a vortex near two circular cylinders. *Proc. R. Soc. Lond.* A **460**, 939–954.

KOZLOV, V. F. 1983 The method of contour dynamics in model problems of the ocean topographic cyclogenesis. *Izv. Atmos. Ocean. Phys.* **19**, 635–640.

KOZLOV, V. F. & MAKAROV, V. G. 1985a Hydrodynamic model for the generation of mushroom-like ocean currents. *Dokl. Akad. Nauk SSSR* **281**, 1213–1215.

KOZLOV, V. F. & MAKAROV, V. G. 1985b Simulation of the instability of axisymmetric vortices using the contour dynamics method. *Fluid Dyn.* **20**, 28–34.

LODER, J. W. & WRIGHT, D. G. 1985 Tidal rectification and frontal circulation on the sides of Georges Bank. *J. Mar. Res.* **43**, 581–604.

LONGUET-HIGGINS, M. S. 1969 On the trapping of wave long-period waves round islands. *J. Fluid Mech.* **37**, 773–784.

LONGUET-HIGGINS, M. S. 1970 Steady currents induced by oscillations round islands. *J. Fluid Mech.* **42**, 701–720.

MACASKILL, C., PADDEN, W. E. P. & DRITSCHEL, D. G. 2003 The CASL algorithm for quasi-geostrophic flow in a cylinder. *J. Comput. Phys.* **188**, 232–251.

MAKAROV, V. G. 1996 Numerical simulation of the formation of tripolar vortices by the method of contour dynamics. *Izv. Atmos. Ocean. Phys.* **32**, 40–49.

MILNE-THOMSON, L. M. 1996 *Theoretical Hydrodynamics*. Dover.

MOREL, Y. G & CARTON, X. J. 1994 Multipolar vortices in two-dimensional incompressible flows. *J. Fluid Mech.* **267**, 23–51.

PEDLOSKY, J., IACONO, R. & NAPOLITANO, E. 2009 The skirted island: the effects of topography on the flow around planetary scale islands. *J. Mar. Res.* **67** (170), 435–478.

PULLIN, D. I. 1992 Contour dynamics methods. *Annu. Rev. Fluid Mech.* **24**, 89–115.

WRIGHT, D. G. & LODER, J. W. 1985 A depth-dependent study of the topographic rectification of tidal currents. *Geophys. Astrophys. Fluid Dyn.* **31**, 169–220.

ZABUSKY, N. J., HUGHES, M. H. & ROBERTS, K. V. 1979 Contour dynamics for the Euler equations in two dimensions. *J. Comput. Phys.* **30**, 96–106.